Possibility of using a tuned inductor in a power device to improve the quality of electricity

MICHAŁ GWÓŹDŹ , RAFAŁ M. WOJCIECHOWSKI ✉

Institute of Electrical Engineering and Electronics
Poznań University of Technology
Piotrowo 3A, 60-965 Poznań, Poland

e-mail: {michal.gwozdz/✉*rafal.wojciewchowski@put.poznan.pl}*

Abstract: This work focuses on the concept of operation and possibility of using a tuned inductor in electrical power systems with adaptive features. The idea presented here for the operation of the inductor is a new approach to the design of such devices. An example of a power adaptive system is a device for improving the quality of electricity. The negative impact of nonlinear loads on the operation of a power grid is a well-documented phenomenon. Hence, various types of "*compensators*" for reactive power, or for both reactive and distortion power, are used in electrical systems as a preventive measure. The concept of an inductor presented here offers wider possibilities for power compensation in power supply systems, compared to traditional solutions involving compensators based on fixed inductors. The use of the proposed solution in an adaptive compensator is only one example of its possible implementation in the area of power devices. In this work, we discuss the structure of the compensator, the basic aspects of the operation of the inductor, the results of simulation studies and the results of measurements obtained from a prototype.

Key words: adaptive compensator, electric energy quality, modelling magnetic elements, tuned inductor

1. Introduction

The negative impact of nonlinear loads on the operation of a power grid, resulting in reduced values of the electrical energy parameters [1], is a widely known and well-documented phenomenon. Hence, various types of "compensators", mainly consisting of (*active and passive*) filters, are used in electrical systems as a preventive measure [2–4]. The main task of these devices is to achieve appropriate matching between the shape of the current at its input and the shape

of the current drawn from the same grid node by other loads. As a result of this compensation process, the current flowing from the power grid to the load should have both a suitable shape and a suitable phase relation with the voltage in the grid node. This process depends on the chosen compensation strategy, relative to either the reactive power or the reactive and distortion power [2, 3, 5].

In the present work, we focus on the concept and possibility of implementation of a tuned inductor (TI) for an adaptive compensator [2, 4, 6], which is one of the main elements of this device. The proposed idea of the operation of a TI is a new approach to the design of power devices with adaptive compensation. In this work, the operation of the adaptive compensator is not related to any specific power theory. Moreover, the use of a TI in compensators is only one example of its possible applications in the area of electrical power systems [7].

The remainder of the paper consists of six sections, which cover the following issues: the structure of the adaptive compensator, the concept of operation of the TI in both a basic and an extended version, the structure of the high-resolution TI, simulation studies of a TI model, and conclusions.

2. Structure of the adaptive compensator

A fixed-parameter compensator improves the power factor of the supply source when the load also has fixed parameters. When these parameters are not constant, the operational effectiveness of such a compensator is lost [8–10], meaning that an adaptive compensator is needed instead. A reactive compensator has adaptive properties if it can be adjusted to changes in the load power. This can be done by switches or through the use of reactive elements with controllable parameters. Adaptive compensators can be built in the form of reactive compensators with semi-controlled devices, such as thyristors, or in the form of switching compensators, which are commonly known as active power filters (APFs) and which use different types of transistors in the power stage of the compensator [2, 4, 6]. However, when the load power is in the range of one tenth of the MVA, as is common in large manufacturing plants, APFs are usually not sufficient. Figure 1(a) shows a block diagram of an electrical system with a generalised adaptive compensator (ACMP) [4].
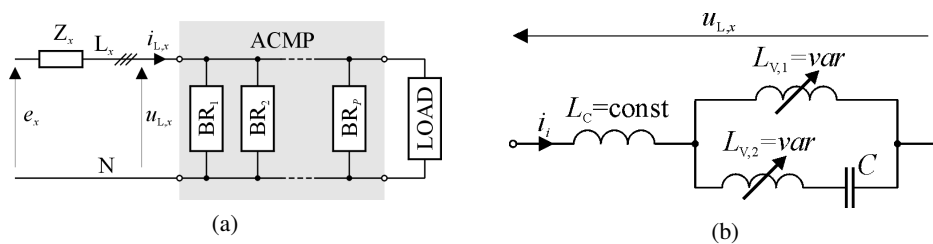

Fig. 1. (a) Block diagram of an electrical system with generalised adaptive compensator, and (b) diagram of the typical topology of a single branch

The ACMP contains P individual branches (BR$_i$) that can be connected in different ways, for example in parallel, as shown in Fig. 1(a). The typical structure of a single branch [2, 4, 5]

is shown in Fig. 1(b). The equivalent impedance of the circuit may vary, as it is composed of variable inductors as follows:

$$\underline{Z}_i = \frac{\underline{U}_{L,x}}{\underline{I}_i} = \text{var} : \quad x = 1, 2, 3,$$ (1)

where x denotes the number of the grid phase.

Typically, saturation of the magnetic core of an inductor enables a change in its inductance [6]. We propose an alternative solution to achieve this effect, which is presented in detail in the following section.

3. Basic operation of a tuned inductor

To implement the TI, a circuit with a magnetically coupled pair of coils was used as shown in Fig. 2. The resultant magnetic flux can be amplified or reduced, which results in a change in the equivalent reactance (X_{TI}) of this circuit, as seen from the power source (i.e. e) side. In the basic version of the inductor, this reactance may have two values, depending on the position of the S-switch.
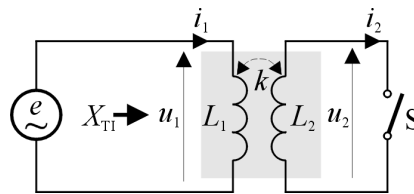
Fig. 2. Diagram showing the principle of operation of a tuned inductor

The value of X_{TI} was calculated based on an analysis of the properties of magnetically coupled circuits. The initial assumptions made did not take into account the nonlinearity of the (*homogeneous*) ferromagnetic core on which the coils were wound. The basic formulae (*assuming a sinusoidal voltage excitation and omitting the resistance of the coils*) describing the voltage and current relations in this circuit are as follows:

$$\underline{U}_1 = jX_1 \underline{I}_1 + jX_M \underline{I}_2 \,,$$ (2)

$$\underline{U}_2 = jX_2 \underline{I}_2 + jX_M \underline{I}_1 \,,$$ (3)

where: X_1, X_2, and X_M are the self- and mutual reactance of the coils, respectively.

As a result of the transformations in (2) and (3), the following formula was obtained for the equivalent reactance of the circuit:

$$jX_{TI} = \frac{\underline{U}_1}{\underline{I}_1} = j\left(X_1 - \frac{X_M^2}{X_2}\right),$$ (4)

in which

$$X_M = k\sqrt{X_1 X_2}\,,$$ (5)

where k is the magnetic coupling factor of the coils and $0 \le k \le 1$.

From (4) and (5), the final equation, in which the value of X_{TI} is dependent on k and the state of the S-switch, is as follows:

$$X_{TI} = \left(1 - S_{T\text{-}TI}k^2\right) X_1 \Big|_{S_{T\text{-}TI}=0 \vee S_{T\text{-}TI}=1} \, , \tag{6}$$

where $S_{T\text{-}TI} = 0$ indicates that the switch is open, and $S_{T\text{-}TI} = 1$ indicates that it is closed.

4. Extended version of the tuned inductor

Our intention was to explore the possibility of a "quasi-smooth" change in the equivalent reactance of the inductor. It was therefore necessary to extend the basic idea of the device, which depended on using a multi-leg magnetic core where the number of legs was equal to $N + 1$ (see, Fig. 3). In each of the N legs, an individual working air gap (labelled $g_1 - g_N$) was inserted, and an individual coil (with a number of turns z, labelled $z_1 - z_N$, respectively) was wound. The circuit was equipped with a total number N of individual switches ($TS_1 - TS_N$). Each single switch was composed of a pair of anti-parallel connected thyristors, and was used to short-circuit the output terminals of the given coil. Hence, the TS_i block responds to the S-switch; the role of the switch was explained in Section 3. As a consequence, the circuit allows us to achieve changes in the value of X_{TI} in 2^N steps:

$$X_{TI} = X_{TI, \text{nom}} \left(1 - \frac{CW}{2^N}\right) : \quad CW = 0, 1, 2, \ldots, 2^{N-1}, \tag{7}$$

where: the subscript "nom" denotes the nominal value of the reactance and CW is the control word for N-bit switches.

The curve in Eq. (6) is illustrated in Fig. 4. This curve is a step-function of the CW. The meanings of the bits in the control word are as follows: "0" denotes that a given switch ($TS_i : i = 0, 1, 2, \ldots, N$) is open, while "1" indicates that it is closed.
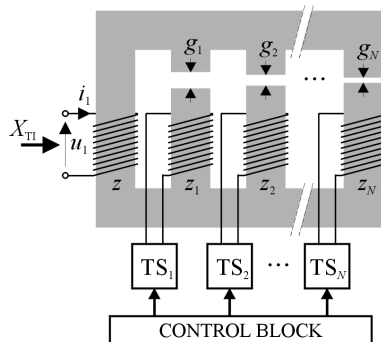

Fig. 3. Structure of the extended version
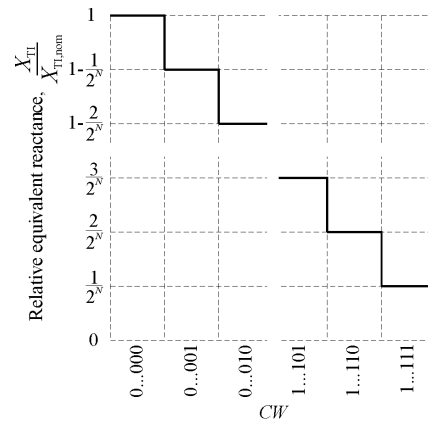of the tuned inductor

Fig. 4. Equivalent relative reactance of the tuned
inductor vs. the control word

In this section, we assume that the implementation of the proposed TI does not require the use of fully controllable power switches, but only semi-controllable ones such as thyristors. These devices switch off naturally after the main current drops to a minimum value, typically as the current waveform passes zero [4]. Hence, no significant commutation overvoltages are expected during the disconnection of the secondary circuit of the TI due to its leakage inductance. In order to confirm this thesis, we performed simulation tests of the circuit shown in Fig. 2 using a model of the real thyristors that were used to replace the ideal S-switch. The results of these tests are shown in Fig. 5. In this case, we used a very simple two-pole R–C circuit, connected to the main terminals of the thyristors switch, as a surge suppressor. The inductance values of the TI were as follows: $X_{\text{TI}} = 20$ mH (S–open); $X_{\text{TI}} = 10$ mH (S–closed).
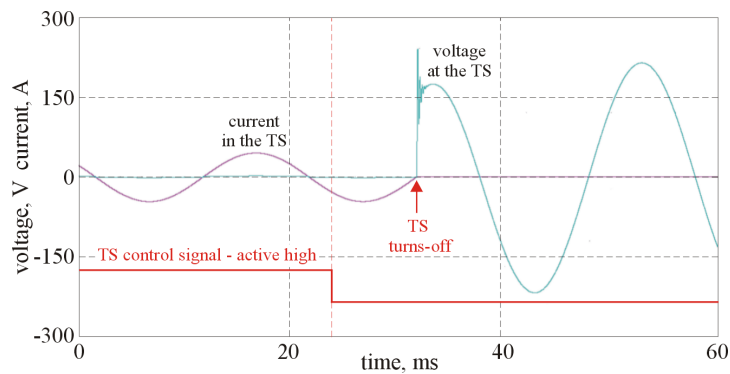

Fig. 5. Results of the simulation tests of the circuit containing the tuned inductor and the thyristor switch

The waveforms show a small overvoltage (*in relation to the supply voltage of the circuit, i.e.* 230 V_{RMS}), when the TS turns off, despite significant values of both the leakage inductance of the TI and the current flowing in this circuit.

5. High-resolution tuned inductor

5.1. Inductor with quasi-smooth changes in the equivalent reactance

In the case where an inductor with high resolution is necessary, the number of its legs can be increased. This makes the design process much longer, as it is more difficult to obtain the assumed inductance values. To simplify this process, we propose a device composed of M individual modules connected in series, each of which is a device with a lower resolution, as shown in Fig. 6.

By appropriately selecting the inductance of the individual modules, it is possible to obtain the same resolution of the inductance as for a single inductor composed of N_i legs. Hence, the tuned inductor parameters are characterised by the following equations, where (8) is in line with the assumption $X_{1,\text{nom}} \gg X_{2,\text{nom}} \gg \ldots \gg X_{M,\text{nom}}$:

$$X_{\text{TI,min}} = \frac{X_{\text{TI,nom}}}{2^K} : K = N_1 + N_2 + \ldots + N_M \,, \tag{8}$$

$$X_{i+1,\max} = \left(1 - \frac{1}{2^{N_i}}\right) X_{i,\min} : \quad i = 1, 2, \ldots, M1, \tag{9}$$

This circuit therefore allows us to achieve a change in the equivalent value of X_{TI} in 2^K steps, similarly to the device based on a complex multi-leg magnetic core described in Section 4.
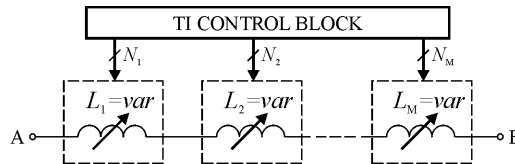

Fig. 6. Structure of a high-resolution modular tuned inductor

It is worth noting that the effect of increasing the resolution of the TI can also be obtained by connecting two of its elements in series (see Fig. 7), where one has a constant inductance and the second a variable inductance. However, in this case, the range of the changes in inductance is limited compared to the solution discussed previously.
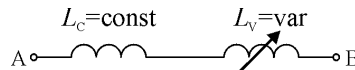

Fig. 7. Inductor composed of fixed and variable inductance parts

5.2. Tuned Inductor with true smooth changes in the equivalent reactance

The following variant of the inductor allows us to continuously tune the equivalent reactance. It requires an active system (i.e. *a power amplifier with input-output galvanic separation*) with a voltage gain of *a* to supply the secondary winding with a voltage which, in terms of shape, is the same as the voltage in the primary circuit (see, Fig. 8). Taking into account (2) and (3), assuming a sinusoidal voltage excitation, and omitting the winding resistances, the operation of this circuit can be described by the following pair of equations:

$$\underline{U}_1 = jX_1 \underline{I}_1 + jX_M \underline{I}_2, \tag{10}$$

$$a\,\underline{U}_1 = jX_2 \underline{I}_2 + jX_M \underline{I}_1, \tag{11}$$
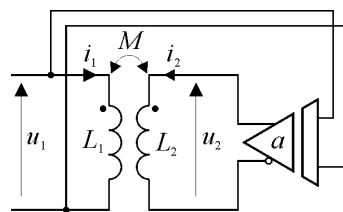
where $0 \leq a \leq 1$.

Fig. 8. Diagram of a inductor circuit with a true smooth value of the equivalent inductance

The proposed solution ensures that we obtain a magnetomotive force in the secondary winding that is identical in shape to that in the primary winding, and hence linearity of the magnetic circuit of the TI (*as before, without taking into account the natural nonlinearity of the core magnetisation characteristic*).

By transforming (10) and (11), we obtain the following relationships describing the basic properties of the inductor:

Equivalent reactance in terms of a and k:

$$X_{\text{TI}} = \frac{\left(1 - k^2\right)}{(1 - ak)} X_1 \,. \tag{12}$$

Minimum value of the equivalent reactance:

$$X_{\text{TI,min}} = \left(1 - k^2\right) X_1 \,. \tag{13}$$

Maximum value of the equivalent reactance:

$$X_{\text{TI,max}} = (1 + k) X_1 \,. \tag{14}$$

Range of the change in the equivalent reactance:

$$\frac{X_{\text{TI,max}}}{X_{\text{TI,min}}} = \frac{1}{1 - k} \,. \tag{15}$$

Value of the gain (a) needed to obtain $X_{\text{TI}} = X_1$:

$$a = k. \tag{16}$$

The dependence of X_{TI} on the voltage gain of the amplifier and the magnetic coupling coefficient of the windings is shown in Fig. 9. These dependencies are highly nonlinear, whereas for a gain value in the range 0.0–0.6 the change in reactance is relatively small. This variant of the TI solution was abbreviated as SWPA (*single secondary winding and power amplifier*). Nevertheless, the modelling of this solution will be carried out in future studies.
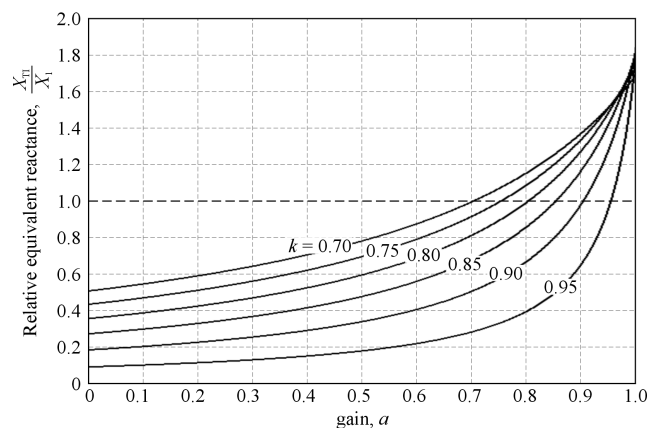

Fig. 9. Dependence of the inductor equivalent reactance on the gain of the amplifier for $k = \text{const}$

6. Simulation modelling of the inductor

Detailed simulation studies of the TI model (*as a single module*) were conducted using our own optimisation software and the Maxwell environment [11]. At this stage of the work, we assumed a value of $N = 2$. These studies showed that to achieve the assumed value of the equivalent inductance, a sophisticated design of the magnetic circuit was necessary. As a result, the model of the inductor was constructed based on a three-winding transformer with working air gaps in the individual legs. To model the construction of the inductor, a 3D field model was employed. For the elaborated model, we used material characteristics from the M270_35A transformer sheet [12]. In the first stage of the design process, in order to obtain the desired values of the parameters in relation to the width of the air gap and the number of turns, we used our own authored software based on the particle swarm optimisation (PSO) algorithm [13, 14] coupled with the magnetic equivalent circuit (MEC) method [15–17]. The initial optimisation of the inductor structure carried out with the use of the MEC model allowed us to narrow the space of decision variables for which the adopted design assumptions of the inductor would be met. When designing the inductor, it was assumed that it would operate at a frequency of 300 Hz, and that the average inductance value in the core would not exceed 1.5 T, meaning that the magnetic circuit would operate within the linear part of the BH curve. Hence, in the first stage of our calculations, we assumed that the core permeability μ_{Fe} = const. On this basis, using dependencies drawn from the theory of magnetic circuits [18], we selected the core cross-section, the heights of the columns and the yokes. However, our attention was mainly focused on optimising the heights of the working slots and the number of turns. We also assumed that the number of turns for each of the coils were the same, i.e. $z = z_1 = z_2$. Searching for optimal values of the decision variables, the following objective function was defined:

$$\Im\left(g_1, g_2, z\right) = \min \left\{ \sum_{TS_2=0}^{1} \left(\sum_{TS_1=0}^{1} \left| \left(1 - \frac{TS_2 + TS_1}{2^N}\right) - \frac{L_{\text{main}}\left(TS_2, TS_1\right)}{L_G}\right| \right) \right\} \Bigg|_{N=2}, \qquad (17)$$

where: g_1 and g_2 represent the heights of the working air gaps; L_G is the sought value of the inductance (here, $L_G = 5$ mH), seen from the side of the terminals of the main winding for switch states $TS_2 = 0$ and $TS_1 = 0$ (i.e. for the state in which both switches are in the *off mode*) and where the terminals of the control windings are open; and $L_{\text{main}}(TS_2, TS_1)$ are the equivalent inductances seen from the terminals of the main winding for various states of the switches TS_1 and TS_2.

While searching for the minimum value of the objective function $I(g_1, g_2, z)$, the values of equivalent inductances $L_{\text{main}}(TS_2, TS_1)$ of the studied inductor were calculated using the proposed MEC model. A view of the structure of the inductor together with its MEC model is shown in Fig. 10. In this model, the reluctances $R_{\mu i}$ relating to individual areas of the core (*i.e. the columns and yokes*) are marked in yellow. The values of these reluctances were calculated using classical formulas known from circuit theory [15]. Blue is used to indicate the reluctances R_{gi} in the areas of the working gaps g_1 and g_2, while green represents the reluctances R_{ri} resulting from the action of the leakage fluxes in the system. When calculating the reluctance values relating to working air gaps, we used formulas based on the Schwarz-Christoffel transformation [15, 16], while the reluctance values were determined using the formula proposed in [17]. The resistances R

of the windings were determined based on the assumed average length of a single turn, the cross-sectional area of the wires and the number of turns for a given case considered in the i-th iterative step of the optimisation process.
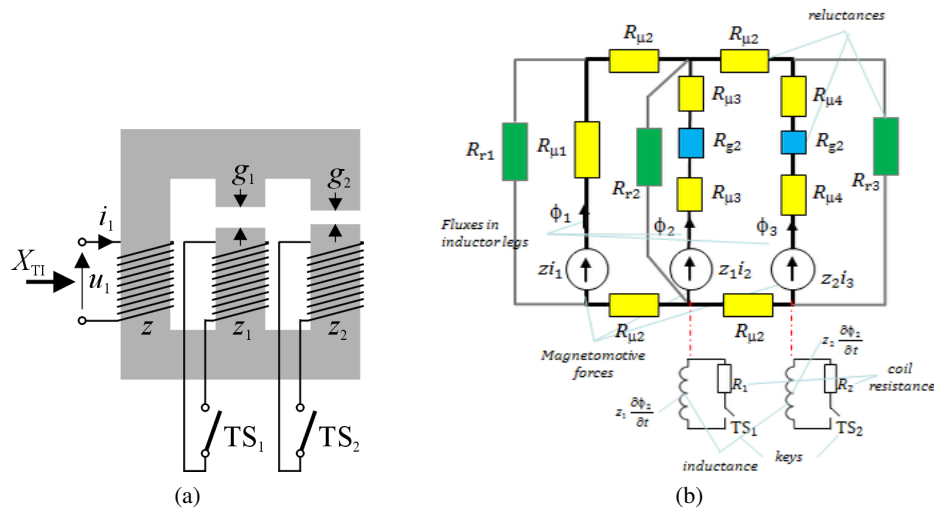

Fig. 10. (a) Structure of the inductor with $N = 2$, (b) MEC model of the inductor

For the circuit formed in this way, we wrote circuit equations describing the distributions of currents and fluxes. These equations were solved with the loop method using complex numbers, by taking into account the current operating states of the switches TS_2 and TS_1. The use of complex calculus allowed us to obtain results directly for the established operating states. On the basis of these results, we calculated the values of the inductances $L_{\text{main}}(TS_2, TS_1)$ for individual sequences of switches, directly from the definition of inductance as the ratio of the flux associated with the main winding ψ_1 ($\psi_1 = z \cdot \varphi_1$) to the value of the current i_1 in this winding, i.e. from the following relation:

$$L_{\text{main}} (TS_2, TS_1) = \left. \frac{\psi_1}{i_1} \right|_{\substack{(TS_2, TS_1) \\ i_1 = 1 \text{ A}}} = \left. \frac{z \cdot \phi_1}{i_1} \right|_{\substack{(TS_2, TS_1) \\ i_1 = 1 \text{ A}}}. \tag{18}$$

Due to the linearity of the magnetic circuit, inductance calculations could be carried out to find the unit value of the current.

As a result of the initial optimisation process, values for the decision variables were obtained that corresponded to the assumptions that were made (i.e. for an idle value of the inductance of $L_G = 5$ mH and maintaining the appropriate proportion between the inductances at the level of ¾, ½ and ¼ for the remaining operating states of the TS2 and TS1 switches). Figure 11 shows the values obtained for the decision variables g_1, g_2 and z. The best result was obtained for the values of $(g_1, g_2, z)|_{\text{opt}} = \{5.09, 1.44, 77\}$, which gave a value for the function of $\Im(g_1, g_2, z) = 0.0235$. The values of the decision variables formed the starting point for the further calculations in the next stage.
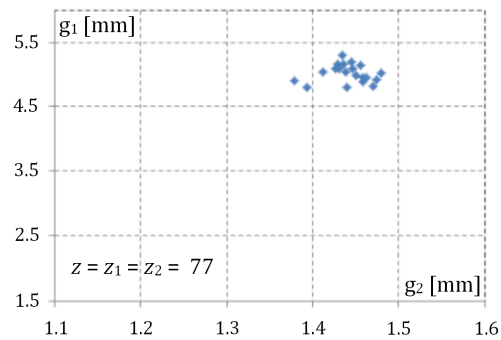
Fig. 11. Values obtained for the decision variables from the optimisation process in the first stage

It should be noted that although the MEC model used is less accurate than field models, it allows for wider spaces for the decision variables in the optimisation process. We used the results of the calculations obtained from the first stage of the design process to select solutions for which the calculated values of the inductances were within the area of the expected values. Finally, we note that the detailed research results from the elaborated optimisation procedures are the subject of another work in preparation, and are not presented here.

In the second stage, verification calculations were carried out for the values obtained for the parameters in the first stage using a 3D field model, as well as a more in-depth optimisation of the construction of the inductor. This time, the calculations were made in the area of selected decision variables obtained in the first stage. In the second stage of the design process, the interval search method was used [19], and was implemented in the optimisation module of Maxwell software, which is based on the popular finite element method (FEM). A 3D view of the inductor model, elaborated in Maxwell software, is shown in Fig. 12, which illustrates the basic technical details of the inductor structure.
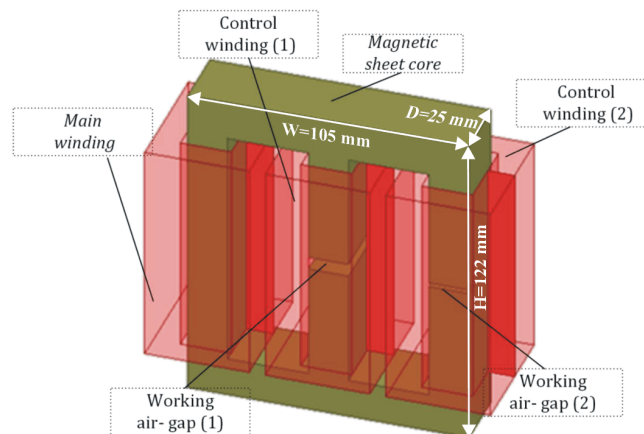

Fig. 12. General view of the simulation model of the tuned inductor

When calculating the values of the self and mutual apparent inductances for the individual windings of the considered inductor, we applied the *frozen permeability method* [20, 21]. In this approach, when the solution to the nonlinear FEM equations for the *j*-th time step has been found, the values of the magnetic permeability μ for the individual finite elements are stored (*frozen*) in PC memory. Then, based on the frozen values of the permittivity μ, the FE equations are solved again for the unit values of the current excitations in the successive windings of the inductor. In this case, these are systems of linear equations. Of the two approaches most commonly used with the frozen permeability method, we employed the method in which values of the self-inductances L_{ii} and mutual inductances L_{ij} are obtained on the basis of the ratio of the flux linkage Ψ_i of the *i*-th winding to the unit values of current I_j in the *j*-th winding:

$$L_{ij} = \Psi_i/I_j \quad \text{for} \quad i, j = 1, 2, 3, \tag{19}$$

where the value "1" represents the main winding, the value "2" represents the first control winding, and the value "3" represents the second control winding.

It should be noted that the *frozen permeability method* allows us to determine the values of the self- and mutual inductances for the individual windings of the studied system. However, from our point of view, the information on the values of the equivalent inductances L_{main} seen from the terminals of the main winding for various states of the switches TS_1 and TS_2 is much more valuable, i.e. $L_{\text{main}}(TS_2, TS_1)$. The values of the equivalent inductance $L_{\text{main}}(TS_2, TS_1)$ were calculated using the following relation:

$$L_{\text{main}}(TS_2, TS_1) = \boldsymbol{e}^T \left[L_{ij} \right] \boldsymbol{s} = \begin{bmatrix} 1 & 0 & 0 \end{bmatrix} \cdot \begin{bmatrix} L_{11} & L_{12} & L_{13} \\ L_{21} & L_{22} & L_{23} \\ L_{31} & L_{32} & L_{33} \end{bmatrix} \cdot \begin{bmatrix} 1 \\ (-1) \cdot TS_1 \\ (-1) \cdot TS_2 \end{bmatrix}, \tag{20}$$

where $\boldsymbol{e}^T$ is the unit vector, $[L_{ij}]$ represents the matrix of inductances, and $\boldsymbol{s}$ is the vector taking into account the relation between the state of a given switch and the sign "–" of the given inductance. The relations in (17) and (18) were used to determine the values of the inductances in the optimisation procedure at the second stage.

A summary of the basic parameters of the simulation model of the TI can be given as follows:
– Core dimensions (H×W×D): 122×105×25 mm.
– Widths of the air gaps: $g_1 = 4.9$ mm, $g_2 = 1.5$ mm.
– Number of turns: $z = z_1 = z_2 = 76$.

Due to the nonlinearity of the magnetic core, the equivalent inductance of the TI varies with the supply voltage, as shown in Fig. 13. These relationships are also dependent on the states of switches used to short-circuit the secondary windings of transformer. The values of the inductances in Fig. 13 were obtained for supply voltage values with a frequency of 300 Hz. The explanation why this value was chosen is that under normal operating conditions, the inductor operates at higher frequencies, which are, typically, odd multiples of the power grid frequency that assumed value was equal to 50 Hz.

The values of the equivalent inductances, which are shown in Fig. 13, were calculated in the Maxwell environment based on the waveforms obtained for the self- and mutual inductances L_{ij} of the windings of the inductor for different amplitudes of the supply voltage. For example, Fig. 14 shows the waveforms of the self- and mutual inductances determined for a voltage with
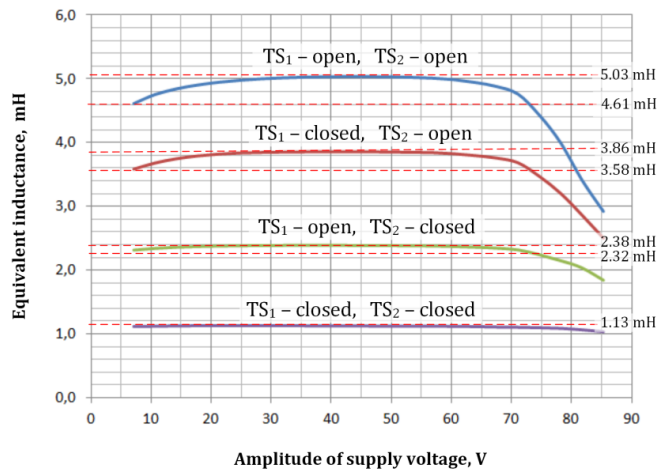
Fig. 13. Equivalent inductance as a function of the amplitude of the supply voltage
to the tuned inductor

amplitude 45 V in the steady state. Then, using the relation in (20), the instantaneous values of the equivalent inductances seen from the side of the main winding terminals were determined for various states of switches TS_1 and TS_2. The waveforms of the inductances $L_{main}(TS_2, TS_1)$ for various states of switches TS_1 and TS_2 are shown in Fig. 15. The values of the inductances obtained for these time steps (i.e. for which the values of the instantaneous current in the main winding reach a maximum) constitute the basis for plotting the relationships in Fig. 15. The decision to choose the inductance value for the maximum value of current in the winding in the
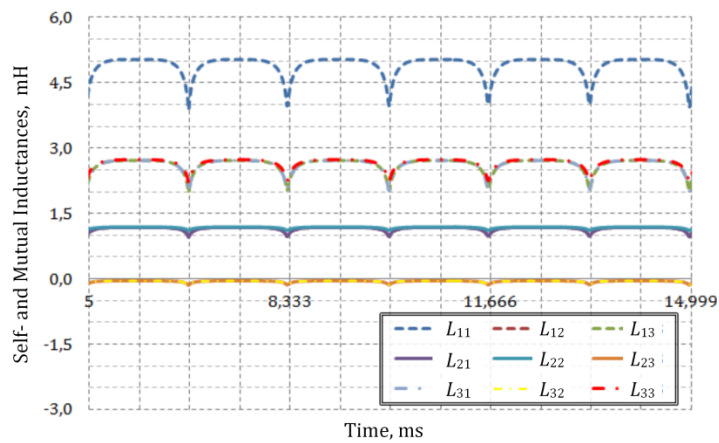

Fig. 14. Waveforms for the self- and mutual apparent inductances of the inductor windings
for a supply voltage of amplitude 45 V

steady state was made due to the possibility of capturing the moment at which the characteristics of the choke enters into the area of saturation.
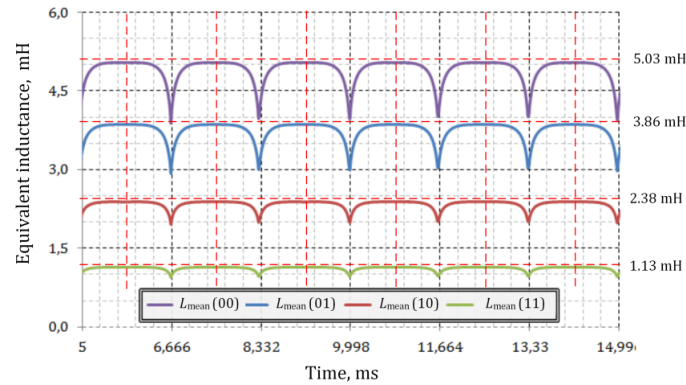

Fig. 15. Waveforms of equivalent inductance as seen from the terminals of the main winding
for a supply voltage of amplitude 45 V

In many inductor applications, it is important that the magnetic core operates in the (quasi-) linear range. Table 1 shows the maximum magnitudes of the main winding current (i_1 in Fig. 2) in this range of the core operation. As expected, the value of this current is strongly dependent on the equivalent inductance of the inductor (i.e. *the particular states of the switches*).

Table 1. Magnitude of the main winding current in the quasi-linear range of core operation

No.	State of switch		CW	Magnitude of current [A]
	TS_2	TS_1		
1.	Open	Open	00	10
2.	Open	Closed	01	15
3.	Closed	Open	10	25
4.	Closed	Closed	11	48

Based on the results obtained from the optimisation and simulations, an inductor prototype was developed, built and tested on a laboratory stand. Figure 16 shows the dependences of the inductances $L_{main}(T_2, TS_1)$ as a function of the amplitude of the supply voltage obtained from the measurements, and a view of the developed TI.

Figure 17 shows the relative values of the inductance of the TI from simulation and measurements, with reference to the theoretical values (given by Eq. (7)). These curves (plotted as *red and blue lines*) are related to the quasi-linear range operation of the inductor (i.e., *assuming a value of* 45 V *for the supply voltage*). The results obtained from both the measurements and the TI simulation indicate that the relative error in the inductance, with reference to the theoretical model, is dependent on the value of the control word and is in the range 2.1–13.6%.
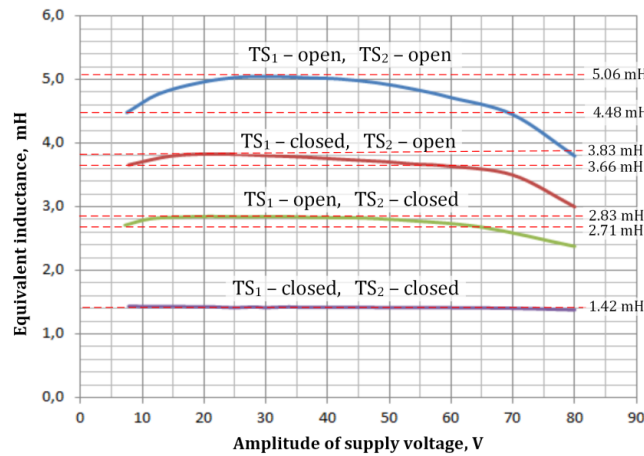
Fig. 16. Equivalent inductance of the tuned inductor as a function of the amplitude
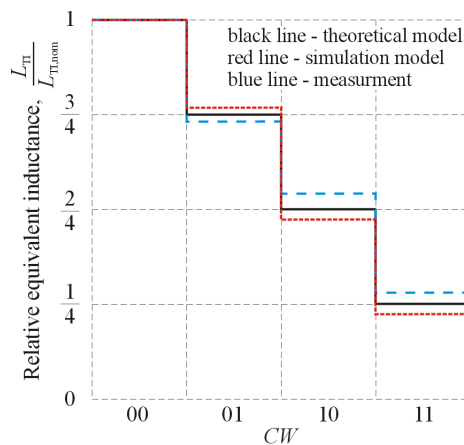of the supply voltage obtained from measurements

Fig. 17. Relative inductance of the tuned inductor from simulation and measurements,
compared to the theoretical assumptions, vs. the control word ($N = 2$)

When designing the TI, we expected that there would be some differences between the calculation results and the measurements. It should be noted that the differences between the results are the result of the technological process adopted (*we employed a fiber laser*) and the lack of accurate information from the manufacturer about the impact of the given method of cutting sheets on the BH curve used for the material. In addition, it can be seen that the applied material exhibits a lower stiffness in the linear part of the of BH curve. However, we see a high compatibility between the results of the calculations and the results for the first prototype of this series. However, Authors believe that they will obtain high compatibility between the results of calculations and results for the first laboratory prototype of the series. This thesis was supported

by the test results of the both 3D field model and laboratory model of a two-leg tunable inductor
(the initial version of the inductor), that were presented in the previous work [7]. In this case,
the discrepancies between inductances of the both models did not exceed 8–10% of the assumed
value – depending on the state of TS switch. Taking into account the theoretical assumptions, the
previous solution for the tuned inductor was very similar to the solution for the device, presented
in the current work.

7. Conclusions

In this work, we have introduced the principle of operation and initial test results for a simu-
lation model of a variable inductance reactor. The results presented here confirm the possibility
of obtaining the required inductance values as a result of controlling the flux in the inductor with
a multi-leg magnetic core with a relative error of no more than 14%. This value can be considered
very satisfactory, taking into account the high complexity of the magnetic circuit of the device.
At the current stage of research, phenomena related to power losses in the core were not analysed
in detail.

This paper explains the principle of operation and presents the results of simulation tests of
a TI based on coupled fluxes, without the need to use the natural nonlinearity of the magnetic
circuit as in most previous studies. In our opinion, the device presented here can be an attractive
solution, particularly for high-power electrical systems, and may include other popular devices
for improving energy quality such as STATCOM and FACTS. However, these applications for
the proposed device need further investigation.

References

[1] Masetti C., *Revision of European Standard EN 50160 on power quality: Reasons and solutions*,
Proceedings of the 14th International Conference on Harmonics and Quality of Power – ICHQP,
Bergamo, Italy (2010), DOI: 10.1109/ICHQP.2010.5625472.

[2] Pasko M., Buła D., Dębowski K., Grabowski D., Maciążek M., *Selected methods for improving
operating conditions of three-phase systems working in the presence of current and voltage deformation
– Part I*, Archives of Electrical Engineering, vol. 67, no. 3, pp. 591–602 (2018), DOI: 10.24425/123665.

[3] Akagi H., Watanabe E.H., Aredes M., *Instantaneous power theory and applications to power condi-
tioning*, John Wiley & Sons: Hoboken, NJ, USA (2017), DOI: 10.1002/9781119307181.

[4] Rashid M.H., *Power Electronics Handbook*, Elsevier Ltd. Oxford (2018).

[5] Qiao X., Bian J., Chen C., Li H., *Comparison and analysis of reactive power compensation strategy
in power system*, Proceedings of IEEE Sustainable Power and Energy Conference (IEEE iSPEC),
pp. 689–692 (2019), DOI: 10.1109/iSPEC48194.2019.8975301.

[6] Czarnecki L., Almousa M., *Adaptive balancing by reactive compensators of three-phase linear loads
supplied by nonsinusoidal voltage from four-wire lines*, American Journal of Electrical Power and
Energy Systems, vol. 10, no. 3, pp. 32–42 (2021), DOI: 10.11648/j.epes.20211003.11.

[7] Gwóźdź M., Wojciechowski R.M., Ciepliński Ł., *Power supply with parallel reactive and distortion
power compensation and tunable inductive filter – Part 2*, Bulletin of the Polish Academy of Sciences,
Technical Sciences, vol. 69, no. 4, pp. 1–9 (2021), DOI: 10.24425/bpasts. 2021.137938.

[8] Trinh Q., Lee H., *An enhanced grid current compensator for grid-connected distributed generation under nonlinear loads and grid voltage distortions*, IEEE Transactions on Industrial Electronics, vol. 61, no. 12, pp. 6528–6537 (2014), DOI: 10.1109/TIE.2014.2320218.

[9] Ye T., Dai N., Zhu M., *Optimize the series LC design of a quasi-proportional-resonant controlled hybrid active power filter for harmonic compensation*, Proceedings of the 11th Conference on Industrial Electronics and Applications (IEEE ICIEA), pp. 624–629 (2016), DOI: 10.1109/ICIEA.2016.7603659.

[10] Lee Y., Song H., *A reactive power compensation strategy for voltage stability challenges in the Korean power system with dynamic loads*, Sustainability, vol. 11, no. 2, p. 326 (2019), DOI: 10.3390/su11020326.

[11] https://www.ansys.com/products/electronics/ansys-maxwell, accessed March 2022.

[12] *Non grain oriented electrical steel powercore*, Thyssenkrupp Steel, https://www.thyssenkrupp-steel.com/media/content_1/publikationen/lieferprogramme/thyssenkrupp_product-range_no-electrical-steel_powercore_steel_en.pdf, accessed March 2022.

[13] Knypiński Ł., Nowak L., Demenko A., *Optimization of the synchronous motor with hybrid permanent magnet excitation system*, COMPEL, vol. 34, no. 2, pp. 448–4552 (2015), DOI: 10.1108/COMPEL-08-2014-0216.

[14] Devarapalli R., Sinha N.K., Venkateswara Rao B., Knypinski Ł., Naga Lakshmi N.J., Márquez F.P.G., *Allocation of real power generation based on computing over all generation cost: Sn approach of salp swarm algorithm*, Archives of Electrical Engineering, vol. 70, no. 2, pp. 337–349 (2021), DOI: 10.24425/aee.2021.136988.

[15] Balakrishnan A., Joines W., Wilson T., *Air-gap reluctance and inductance calculations for magnetic circuits using a Schwarz-Christoffel transformation*, Proceedings of PESC '95 – Power Electronics Specialist Conference, vol. 2, pp. 1050–1056 (1995), DOI: 10.1109/PESC.1995.474945.

[16] Zhang X., Xiao F., Wang R., Fan X., Wang H., *Improved calculation method for inductance value of the air-gap inductor*, Proceedings of the 1st China International Youth Conference on Electrical Engineering (IEEE CIYCEE), pp. 1–6 (2020), DOI: 10.1109/CIYCEE49808.2020.9332553.

[17] Yang Y., Ma J., Ho C., Zou Y., *A new coupled-inductor structure for interleaving bidirectional DC-DC converters*, IEEE Journal of Emerging and Selected Topics in Power Electronics, vol. 3, no. 3, pp. 841–849 (2015), DOI: 10.1109/JESTPE.2015.2443178.

[18] Dubois H., *Magnetic circuit in theory and practice*, Book (2015), Nabu Press Publisher.

[19] Chong E., Zak S., *An introduction to optimization*, 4th edition, Wiley Publishing (2013).

[20] Escarela-Perez R., Campero-Littlewood E., Arjona-Lopez M., Laureano-Cruces A., *Comparison of two techniques for two-dimensional finite-element inductance computation of electrical machines*, IEEE Proceedings – Electric Power Applications, vol. 152, no. 4, pp. 855–861 (2005), DOI: 10.1049/ip-epa:20055242.

[21] Fouad F., Nehl T., Demerdash N., *Saturated transformer inductances determined by energy perturbation techniques*, IEEE Transactions on Power Apparatus and Systems, vol. PAS-101, no. 11 (1982), DOI: 10.1109/TPAS.1982.317363.